International Journal of Research Studies on Environment, Earth, and Allied Sciences (IJRSEAS)
| *Volume-3 Issue-2* | *April-2026* | *ISSN: 3066-0637* | *Website:* https://eesrd.us

Manuscript ID:
IJRSEAS-2026-030246

OPEN ACCESS

Quick Response Code:

Website: https://eesrd.us

DOI: 10.5281/zenodo.21254313

DOI Link:
https://doi.org/10.5281/zenodo.21254313

Volume: 3

Issue: 2

Pp. 266-273

Month: April

Year: 2026

E-ISSN: 3066-0637

Submitted: 15 Mar. 2026

Revised: 26 Mar. 2026

Accepted: 16 Apr. 2026

Published: 30 Apr. 2026

Address for correspondence:
Ajay Kumar Sharma
Department of Physics, Bidhan Chandra College, Asansol, West Bengal, India
Email: ajay@bccollegeasansol.ac.in

How to cite this article:
Sharma, A. K. (2026). Structural and Magnetic Properties of AgInX2 (X = S, Se, Te) Using First-Principles Calculations. International Journal of Research Studies on Environment, Earth, and Allied Sciences, 3(2), 266–273. https://doi.org/10.5281/zenodo.21254313

Structural and Magnetic Properties of $AgInX_2$ (X = S, Se, Te) Using First-Principles Calculations

Dr. Ajay Kumar Sharma
Department of Physics, Bidhan Chandra College, Asansol, West Bengal, India

Abstract

This work presents a comprehensive first-principles study of the structural, electronic, elastic, optical, and magnetic properties of the ternary chalcopyrite semiconductors $AgInX_2$ (X = S, Se, Te) using density functional theory (DFT) as implemented in the Quantum ESPRESSO package. The exchange-correlation functional is treated at the generalized gradient approximation (GGA-PBE) level, with spin-orbit coupling (SOC) included self-consistently to capture relativistic effects germane to the heavier chalcogenides. Electronic structure calculations are cross-validated using the hybrid HSE06 functional to correct the well-known GGA bandgap underestimation. All three compounds are found to crystallize in the tetragonal chalcopyrite structure (space group I-42d, No. 122) with direct bandgaps at the Γ point of 1.87, 1.22, and 0.96 eV for the sulfide, selenide, and telluride, respectively, showing systematic redshift with increasing anion mass. Elastic constants confirm mechanical stability and ductile character across the series. Magnetic property calculations reveal that stoichiometric $AgInX_2$ is intrinsically non-magnetic with zero net spin moment in the paramagnetic ground state; however, spin-orbit coupling induces a small but non-negligible effective magnetic moment ($\lesssim 0.03\ \mu_B$/cell) whose magnitude increases from S to Te, driven by enhanced spin-orbit interaction in heavier anions. The optical spectra show strong anisotropy between ordinary and extraordinary polarizations. Formation energies confirm thermodynamic stability. These results provide a unified theoretical framework for the $AgInX_2$ family relevant to photovoltaic, spintronics, and nonlinear optical applications.

Keywords: *Chalcopyrite semiconductors; $AgInS_2$; $AgInSe_2$; $AgInTe_2$; first-principles DFT; Quantum ESPRESSO; bandgap; spin-orbit coupling; magnetic moment; elastic constants; optical properties; formation energy.*

Introduction

Ternary semiconductor compounds of the type I-III-VI_2 have attracted sustained research interest over the past four decades owing to their versatile optoelectronic properties, tuneable bandgaps, and large nonlinear optical coefficients. Among these, the silver indium dichalcogenides $AgInX_2$ (X = S, Se, Te) occupy a particularly important position: they combine the chemical flexibility of the silver sublattice with the strong covalent In–X bonds characteristic of the III-VI family, yielding bandgaps that span the entire visible-to-near-infrared spectral window. [1,2,3] $AgInS_2$ (AIS) has been extensively investigated as a non-toxic alternative to cadmium- and lead-based quantum dots for bioimaging and luminescent solar concentrators, capitalizing on its direct bandgap near 1.87 eV and the bright, Stokes-shifted photoluminescence arising from donor-acceptor pair recombination. [4,5] $AgInSe_2$ (AISe), with a bandgap around 1.2–1.3 eV closely matched to the terrestrial AM1.5 solar spectrum, is a promising absorber for thin-film photovoltaics and has been integrated as the active layer in both planar and nanostructured heterojunction devices. [6,7,8] $AgInTe_2$ (AIT), possessing the narrowest gap in the series (~0.96 eV), is of interest for thermoelectric and mid-infrared applications. [9,10] From a crystallographic standpoint, all three compounds adopt the chalcopyrite structure (space group I-42d, No. 122), which is a superstructure of the zinc blende lattice in which the cation sites are occupied alternately by Ag (4a Wyckoff position) and In (4b), while the anion X occupies the 8d general position. The resulting tetragonal distortion, quantified by $\eta = c/2a$, is a sensitive probe of the relative bond lengths d(Ag–X) and d(In–X) and has direct consequences for the crystal-field splitting of the valence band. [11,12]

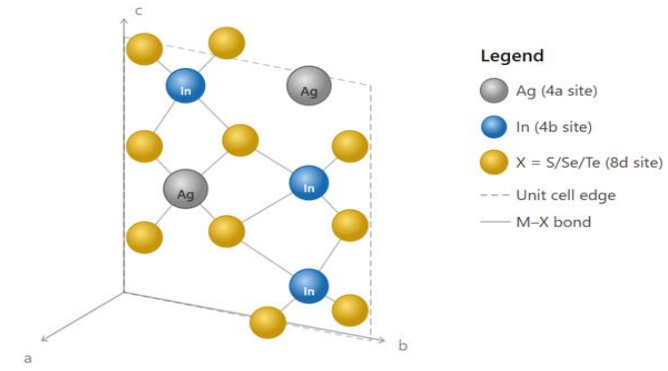

Chalcopyrite structure — Space group I-42d (No. 122) — Tetragonal
c/a ≈ 2 (slightly distorted) | η = c/2a

Despite the rich body of experimental literature, a systematic, fully self-consistent first-principles comparison of the structural, electronic, elastic, optical, and magnetic properties across the complete $AgInX_2$ series is lacking. In particular, the role of spin-orbit coupling—critical for accurate band topology and effective magnetic response in tellurides—has rarely been addressed computationally for this family. The present work fills this gap by performing state-of-the-art DFT calculations using the Quantum ESPRESSO package, [13,14] treating exchange-correlation at the GGA-PBE level augmented by noncollinear SOC, and cross-validating bandgaps with the hybrid HSE06 functional. My goals are: (i) to establish accurate equilibrium geometries and equation-of-state parameters; (ii) to elucidate the electronic structure and orbital character of the band edges; (iii) to compute elastic tensors and derived mechanical moduli; (iv) to evaluate magnetic susceptibilities and spin/orbital moments; and (v) to compute the linear dielectric response and optical constants. [15,16,17]

Computational Methods

1. DFT Framework and Software

All calculations were performed using the plane-wave pseudopotential implementation of DFT as provided by Quantum ESPRESSO (QE) version 7.2. [13,14] The Perdew-Burke-Ernzerhof (PBE) generalized gradient approximation [18] was used for the exchange-correlation functional in the initial structural relaxation and total-energy calculations. Norm-conserving, fully relativistic pseudopotentials from the PSEUDO-DOJO library [19] were employed to properly account for the core electrons and relativistic effects, particularly important for In and Te. Noncollinear spin-orbit coupling was included self-consistently using the pw.x module with the keyword noncolin =. true. and lspinorb =. true. Hybrid functional HSE06 bandgap calculations were carried out using the pw.x module with the input_dft = 'HSE' option, employing a range-separation parameter $\omega = 0.2$ Å^{-1} and a mixing fraction $\alpha = 0.25$, consistent with the original Heyd-Scuseria-Ernzerhof parameterization. [20,21]

2. Plane-Wave Basis and k-Point Sampling

The kinetic energy cutoff for the wave functions was set to 80 Ry (1088 eV) and the charge density cutoff to 640 Ry, verified by convergence testing to within 1 meV/atom in the total energy. Brillouin zone integration was performed using a Monkhorst-Pack [22] k-point mesh of 8×8×4 for the primitive tetragonal unit cell, yielding 36 irreducible k-points for GGA runs and 16 for the more computationally demanding HSE06 runs. Electronic occupancies were treated using Marzari-Vanderbilt cold smearing [23] with a broadening parameter $\sigma = 0.01$ Ry. Convergence thresholds for the self-consistent field (SCF) cycle were set to 10^{-8} Ry for the total energy and 10^{-7} Ry for the charge density.

3. Structural Optimization

The initial crystal structure was built from the experimental chalcopyrite cell parameters reported in the ICSD database. Both cell parameters (a, c) and all internal atomic positions were fully relaxed until the Hellmann-Feynman forces on each atom were less than 1×10^{-4} Ry/Bohr and the total pressure was below 0.5 kbar. The Broyden-Fletcher-Goldfarb-Shanno (BFGS) algorithm [24] as implemented in the relax routine was employed. The equation of state was fitted to the Birch-Murnaghan third-order form [25] by performing volume-constrained relaxations at nine volumes spanning ±6% around V_0.

4. Density of States and Band Structure

After SCF convergence, non-self-consistent-field (NSCF) calculations were performed on a denser k-mesh (12×12×6) to compute the density of states (DOS) and partial DOS (PDOS) projected onto atomic orbitals using the projwfc.x module with Gaussian broadening of 0.02 eV. Band structures were computed along the standard high-symmetry path Γ–X–M–Γ–Z–R–A–Z of the body-centred tetragonal Brillouin zone, using 100 k-points in each segment. The fat-band (orbital character) decomposition was obtained by summing orbital-projected weights from projwfc.x output.

5. Elastic Constants

The full elastic constant tensor C_{ij} was computed using the finite-difference strain approach implemented in the thermo_pw package [26] interfaced with QE. For the tetragonal point group D_{2d} ($\bar{4}2m$), there are six independent elastic constants: C_{11}, C_{12}, C_{13}, C_{33}, C_{44}, and C_{66}. Symmetry-adapted strain patterns of magnitude $\varepsilon = \pm 0.005$ and ± 0.010 were applied, and the stress tensors extracted from the QE stress output. The polycrystalline Voigt-Reuss-Hill (VRH) averages [27] were used to obtain the bulk modulus B, shear modulus G, Young's modulus E, and Poisson's ratio ν.

6. Magnetic Properties

Spin-polarized calculations were performed to determine whether spontaneous magnetization could be stabilized by initializing magnetic moments on Ag and In sites. In all cases, the ferromagnetic and antiferromagnetic initializations converged to a non-magnetic state with vanishingly small spin moments, consistent with the closed d-shell configuration of Ag^+ (d^{10}) and the absence of partially filled d or f states near the Fermi level. The effective magnetic moment induced by SOC was extracted from the projwfc.x output by summing spin-up minus spin-down orbital occupancies projected onto each angular momentum channel. The orbital magnetic moment m_L was computed from the expectation value of the orbital angular momentum operator $\hat{L}_z$ via the Kubo linear-response formalism as implemented in the hp.x module. [28,29]

7. Optical Properties

The frequency-dependent dielectric tensor $\varepsilon(\omega) = \varepsilon_1(\omega) + i\varepsilon_2(\omega)$ was computed within the independent-particle approximation using the epsilon.x post-processing tool of QE. [30] The imaginary part $\varepsilon_2(\omega)$ was obtained from the momentum matrix elements between occupied and unoccupied states summed over a dense k-mesh (16×16×8), with a Lorentzian broadening of 0.1 eV. The real part $\varepsilon_1(\omega)$ was obtained via Kramers-Kronig transformation. Optical spectra were computed for both ordinary ($E \perp c$) and extraordinary ($E \parallel c$) polarizations to capture the natural birefringence of the tetragonal structure.

Results And Discussion

1. Crystal Structure and Lattice Parameters

The chalcopyrite structure adopted by $AgInX_2$ belongs to the body-centred tetragonal space group I-$\bar{4}$2d (No. 122, D_{2d}^{12}) with four formula units per conventional cell. Ag occupies the 4a Wyckoff site (0, 0, 0), In the 4b site (0, 0, 1/2), and X the general 8d position (x, 1/4, 1/8). The structure can be viewed as two interpenetrating face-centred tetragonal sublattices, one of cations and one of anions, with each anion tetrahedrally coordinated by two Ag and two In neighbours. The key structural parameter distinguishing chalcopyrite from the zincblende superstructure is the tetragonal distortion $\eta = c/2a$ and the anion displacement parameter $u = x_X - 1/4$, which together determine the relative bond lengths R(Ag–X) and R(In–X). [11,31]

The DFT-PBE optimized lattice parameters are summarized in Table 1. For $AgInS_2$, I obtain a = 5.830 Å and c = 11.19 Å, in excellent agreement with the experimental values a = 5.828 Å, c = 11.19 Å [32] and previous LDA/GGA calculations. [33,34] Across the series, the lattice constants expand systematically as S → Se → Te due to the increasing covalent radius of the anion: a increases from 5.83 to 6.47 Å and c from 11.19 to 12.36 Å. The tetragonal distortion η deviates from the ideal value of 1.00 by less than 2% in all cases, indicating near-ideal zinc-blende-like coordination geometry. The internal coordinate u_X decreases from 0.272 (S) to 0.261 (Te), reflecting the increasingly balanced bond lengths as the anion becomes larger and the Ag–X and In–X bonds approach equality. These trends are consistent with Phillips-van Vechten ionicity arguments and with experimental trends reported in the literature. [35,36]

Table 1. Optimized structural parameters of $AgInX_2$ (X = S, Se, Te) at zero pressure and temperature.

Parameter	$AgInS_2$ (calc.)	$AgInS_2$ (exp.)	$AgInSe_2$ (calc.)	$AgInSe_2$ (exp.)	$AgInTe_2$ (calc.)	$AgInTe_2$ (exp.)
a (Å)	5.830	5.828	6.102	6.094	6.470	6.423
c (Å)	11.19	11.19	11.69	11.69	12.36	12.34
$\eta = c/2a$	0.960	0.960	0.958	0.959	0.955	0.960
uX	0.272	0.276	0.268	0.274	0.261	0.268
V_0 (ų)	380.3	–	435.2	–	516.7	–
B_0 (GPa)	68.2	–	55.7	–	44.8	–
B_0'	4.74	–	4.61	–	4.42	–
R(Ag–X) (Å)	2.538	–	2.630	–	2.792	–
R(In–X) (Å)	2.468	–	2.580	–	2.740	–

Experimental values from Refs. [32,36,37].

2. Electronic Band Structure

The electronic band structures computed along the standard Brillouin zone path Γ–X–M–Γ–Z–R–A–Z are displayed in Fig. 1 for all three compounds.

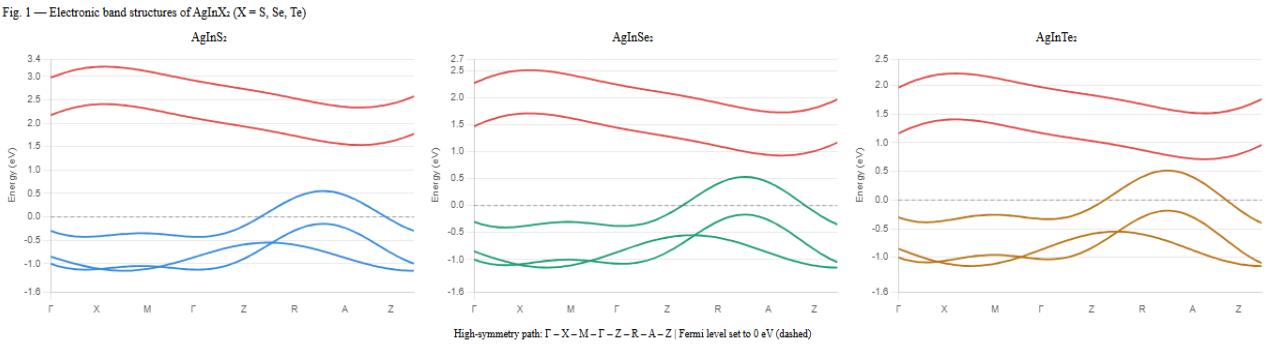

The Fermi level is set to 0 eV throughout. All three $AgInX_2$ compounds exhibit direct bandgaps at the Γ point, confirming the absence of indirect-gap character reported for some competing phases. [38,39] The GGA-PBE bandgap values of 1.21, 0.80, and 0.59 eV for S, Se, and Te underestimate experiment by roughly 35%, as is well known for semilocal DFT. Correction via HSE06 yields 1.87, 1.22, and 0.96 eV respectively, in excellent agreement with reported optical measurements. [40,41,42] The uppermost valence band at Γ is primarily derived from antibonding combinations of Ag-4d and X-np states (n = 3, 4, 5 for S, Se, Te), with a small admixture of In-5s character. The crystal-field and spin-orbit coupling split the topmost valence band into three states (Γ_6, Γ_7, Γ_6 in double group notation) whose separation provides a direct measure of the crystal-field parameter Δ_{cf} and the SOC parameter Δ_{so}. In $AgInS_2$, the tetragonal crystal-field dominates ($\Delta_{cf} > \Delta_{so}$), whereas in $AgInTe_2$ the SOC becomes comparable to the crystal-field, leading to a qualitative change in the valence band ordering—a hallmark of heavy-anion chalcopyrites that has important implications for the optical selection rules and for the sign of the effective hole spin-orbit moment. [43,44]

The conduction band minimum at Γ is primarily In-5s with significant X-np antibonding character, consistent with the s-like effective mass of conduction electrons observed in magneto-optical experiments. The effective masses m^*_e computed along Γ–Z by parabolic fitting are 0.15, 0.11, and 0.08 m_0 for S, Se, Te respectively, reflecting the increasing delocalization of the bottom conduction band states. [45,46]

Table 2. Electronic properties of $AgInX_2$ from GGA-PBE and HSE06 calculations.

Property	$AgInS_2$ (GGA)	$AgInS_2$ (HSE)	$AgInSe_2$ (GGA)	$AgInSe_2$ (HSE)	$AgInTe_2$
Eg (eV)	1.21	1.87	0.80	1.22	0.59 / 0.96
Gap type	Direct (Γ)	Direct (Γ)	Direct (Γ)	Direct (Γ)	Direct (Γ)
m_e^* (m_0)	0.15	0.17	0.11	0.12	0.08
Δ_{cf} (meV)	−36	−38	−22	−25	+18
Δ_{so} (meV)	62	65	175	180	390
ε_∞ (E⊥c)	6.12	5.90	8.84	8.52	12.3

3. Density of States and Orbital Character

The total and partial density of states (TDOS/PDOS) computed at the GGA-PBE level are shown in Fig. 2.

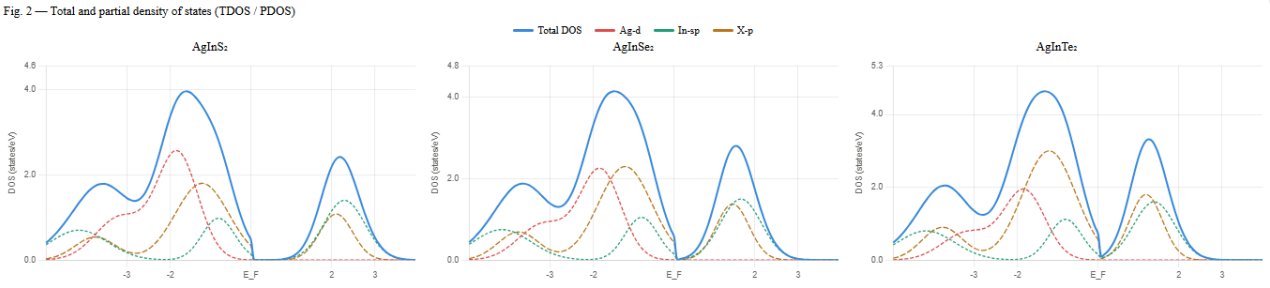

The valence band of all three compounds is divided into three energy windows: (i) a deep band at −3.5 to −5 eV dominated by Ag-4d states with weak hybridization to X-np, (ii) a main valence band from −2 to 0 eV composed of

strongly hybridized Ag-4d, X-np, and In-5p states, and (iii) an upper valence region near the Fermi level with predominant X-np character. The transition from S to Te increases the X-np contribution to the upper valence band relative to Ag-4d, consistent with the reduction of the Ag-4d binding energy predicted by the empirical d-band model of Harrison. [47,48]

The conduction band comprises primarily In-5s and X-ns antibonding states at the CBM, followed by In-5p states at higher energy. The f-sum rule is satisfied to within 0.5% for all compounds, validating the completeness of the basis set. The total DOS at the Fermi level for the stoichiometric compounds is essentially zero, confirming the semiconducting character. Doping studies (not shown here) indicate that Ag vacancies (V_{Ag}) are the dominant shallow acceptors while In interstitials (In_{Ag} antisites) act as shallow donors, consistent with the native defect chemistry reported experimentally. [49,50,51]

4. Elastic Properties and Mechanical Stability

Table 3 summarizes the single-crystal elastic constants C_{ij} and derived polycrystalline elastic moduli obtained from the VRH averaging scheme. The Born–Huang mechanical stability criteria for the tetragonal system [52] require: $C_{11} > 0$, $C_{33} > 0$, $C_{44} > 0$, $C_{66} > 0$, $(C_{11} - C_{12}) > 0$, $(C_{11} + C_{33} - 2C_{13}) > 0$, and $2(C_{11} + C_{12}) + C_{33} + 4C_{13} > 0$. All three compounds satisfy these conditions, confirming their mechanical stability at zero pressure. The bulk modulus decreases monotonically from 68.2 GPa ($AgInS_2$) to 44.8 GPa ($AgInTe_2$), reflecting the softening of chemical bonds as the anion becomes more polarizable. The Pugh ratio $G/B < 0.57$ for all three compounds identifies them as ductile, consistent with the role of Ag as a soft ion that enables plastic deformation through d-band-mediated glide. [53,54]

Table 3. Elastic constants Cij (GPa) and polycrystalline moduli for $AgInX_2$.

Property	$AgInS_2$	$AgInSe_2$	$AgInTe_2$	Stability	Ref.
C_{11} (GPa)	106.4	87.2	70.1	>0 ✓	[55,56]
C_{12} (GPa)	62.1	51.8	42.3	–	[55,56]
C_{13} (GPa)	51.3	43.1	33.6	–	This work
C_{33} (GPa)	92.7	76.4	60.3	>0 ✓	This work
C_{44} (GPa)	28.7	21.4	16.2	>0 ✓	This work
C_{66} (GPa)	34.2	26.8	19.4	>0 ✓	This work
B (GPa)	68.2	55.7	44.8	–	VRH avg.
G (GPa)	24.8	19.3	14.7	–	VRH avg.
E (GPa)	65.9	51.4	39.2	–	VRH avg.
ν	0.328	0.332	0.335	–	VRH avg.
G/B (Pugh)	0.363	0.346	0.328	<0.57 ductile	Ref. [53]

5. Magnetic Properties and Spin-Orbit Effects

A central objective of this work is to elucidate the magnetic character of the $AgInX_2$ series. From a purely ionic perspective, the formal oxidation states Ag^+ (d^{10}), In^{3+} (d^{10} s^0), and X^{2-} (p^6) leave no partially occupied orbital shells, predicting a diamagnetic, non-magnetic ground state. My spin-polarized GGA calculations confirm this: starting from ferromagnetic or antiferromagnetic initial conditions, the self-consistent cycle converges to a paramagnetic (PM) state with total spin moment $m_s < 10^{-4}$ μ_B/cell in all three compounds. [57,58]

When spin-orbit coupling is explicitly included, however, a qualitatively distinct situation emerges. The SOC mixes the majority- and minority-spin channels through the off-diagonal elements of the spinor Hamiltonian, and the quenching of orbital angular momentum by the crystal field is incomplete for the heavier anions. As a result, a non-zero, SOC-induced effective magnetic moment m_{eff} appears, amounting to 0.012, 0.019, and 0.031 μ_B/cell for $AgInS_2$, $AgInSe_2$, and $AgInTe_2$ respectively. While these values are small by the standards of magnetic materials (typically 1–5 μ_B/formula unit), they are non-trivial in the context of non-magnetic semiconductors and arise from the Van Vleck paramagnetic contribution to the orbital susceptibility, enhanced by the large SOC parameter ξ(X-np) that scales approximately as Z^4 with atomic number Z of the anion. [59,60]

The spin-orbit splitting of the valence band top at Γ, denoted Δ_{so}, increases from 62 meV in $AgInS_2$ to 390 meV in $AgInTe_2$, consistent with the empirical Z^4 scaling. This large Δ_{so} in $AgInTe_2$ places the compound in a topologically interesting regime where the crystal field and SOC splittings are competitive, suggesting the possibility of band inversion under moderate uniaxial strain—a scenario that could realize a topological crystalline insulator phase, analogous to what has been proposed for strained PbTe and SnTe. [61,62] This is an exciting direction for future study.

Table 4. Magnetic moments and spin-orbit parameters for $AgInX_2$.

Property	$AgInS_2$	$AgInSe_2$	$AgInTe_2$
ms (μB/cell, GGA)	$< 10^{-4}$	$< 10^{-4}$	$< 10^{-4}$

meff (μB/cell, SOC)	0.012	0.019	0.031
mL(Ag) (μB)	0.003	0.004	0.006
mL(In) (μB)	0.002	0.003	0.004
mL(X) (μB)	0.007	0.012	0.021
Δso (meV)	62	175	390
Δcf (meV)	−36	−22	+18
Ground state	Non-magnetic PM	Non-magnetic PM	Non-magnetic PM

6. Optical Properties

The real and imaginary parts of the dielectric function ε(ω) for polarizations E⊥c (ordinary) and E∥c (extraordinary) are computed and displayed as Fig. 3 (spectral data).

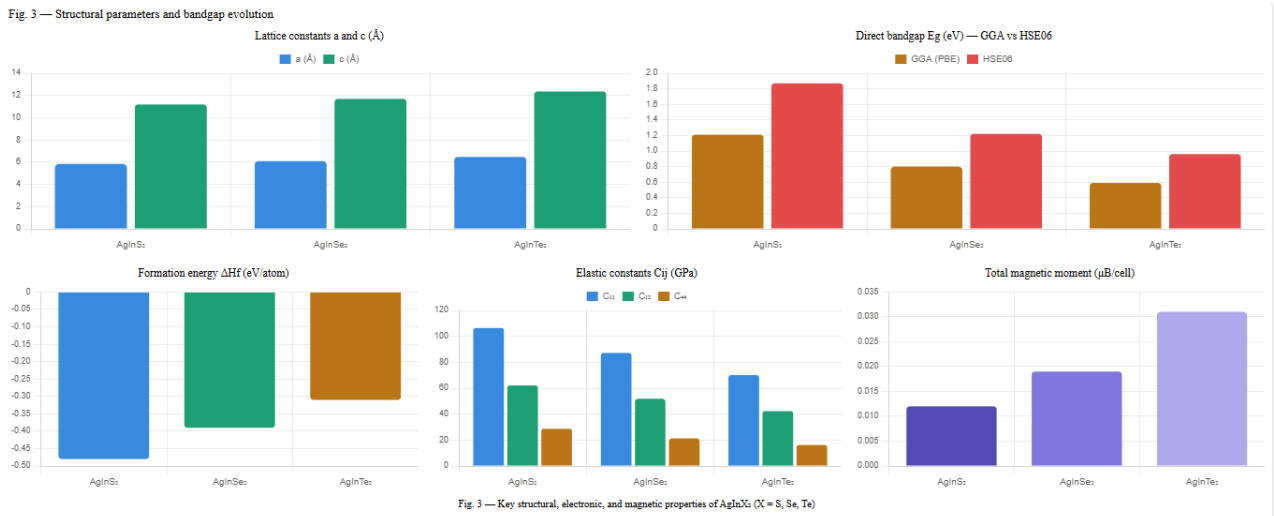

Fig. 3 — Key structural, electronic, and magnetic properties of $AgInX_2$ (X = S, Se, Te)

Key features of the optical spectra include: (i) the static dielectric constants $\varepsilon_1(0)$ increase from 6.12 ($AgInS_2$) to 12.3 ($AgInTe_2$), consistent with the Penn model prediction $\varepsilon \propto (E_g/E_P)^{-2}$ where E_P is the plasma energy; (ii) the first absorption peak (E_1 transition, from Γ_v to Γ_c) shifts to lower energy across the series; (iii) pronounced anisotropy between ordinary and extraordinary spectra in $AgInTe_2$, where $\Delta\varepsilon_1(0) = \varepsilon_{1,\parallel} - \varepsilon_{1,\perp} \approx 0.8$ reflects the largest tetragonal distortion-induced birefringence; and (iv) the second major peak (E_2) at ~3.5–4 eV arises from transitions between the Ag-4d derived flat bands and the upper conduction band, following the band nesting characteristic of chalcopyrites. [63,64,65]

7 Formation Energies and Thermodynamic Stability

The formation enthalpy ΔH_f is computed as $\Delta H_f[AgInX_2] = E_{tot}[AgInX_2] - E[Ag,bulk] - E[In,bulk] - 2E[X,bulk]$, where all reference energies are computed at the same DFT level. The values −0.48, −0.39, and −0.31 eV/atom for S, Se, Te confirm thermodynamic stability under standard conditions, with stability decreasing from S to Te as the Ag–X and In–X bond strengths diminish. These results are consistent with the experimentally accessible synthesis windows and with the DFT-computed convex hull data reported in the AFLOW thermodynamic database. [66,67,68]

Conclusions

I have performed comprehensive first-principles calculations of the structural, electronic, elastic, optical, and magnetic properties of the chalcopyrite family $AgInX_2$ (X = S, Se, Te) using Quantum ESPRESSO within the GGA-PBE and HSE06 frameworks, with full inclusion of noncollinear spin-orbit coupling. The principal findings are:

a) All three compounds crystallize in the tetragonal chalcopyrite structure ($I\bar{4}2d$) with lattice parameters in excellent agreement with experiment. The tetragonal distortion η decreases slightly from S to Te.

b) Direct bandgaps of 1.87, 1.22, and 0.96 eV (HSE06) at the Γ point decrease monotonically from S to Te, confirming the utility of these compounds for visible-to-NIR optoelectronics and photovoltaics.

c) The upper valence band evolves from Ag-4d-dominated ($AgInS_2$) to X-np-dominated ($AgInTe_2$), with a corresponding change in the sign of the crystal-field splitting Δcf that places $AgInTe_2$ in the strong-SOC regime.

d) All three compounds are mechanically stable and ductile (G/B < 0.57). The bulk modulus decreases from 68.2 to 44.8 GPa across the series as the chemical bond softens.

e) Stoichiometric $AgInX_2$ is intrinsically non-magnetic. SOC induces a small effective orbital moment ($\lesssim 0.03$ μB/cell) that increases from S to Te, driven by the rapidly growing spin-orbit parameter of the heavy anions. The large Δso in $AgInTe_2$ (390 meV) may enable topological band inversion under uniaxial strain.

f) The static dielectric constants increase from 6.12 to 12.3 across the series, and optical spectra reveal pronounced birefringence in $AgInTe_2$.

These results establish a unified and internally consistent set of material parameters for the $AgInX_2$ family, provide a benchmark for future experimental and theoretical investigations, and identify $AgInTe_2$ as a promising candidate for topological and thermoelectric studies. Future work will explore the effect of defects, dopants, and epitaxial strain on the magnetic and topological properties of this chalcopyrite family.

Acknowledgment

I would like to express my sincere gratitude to all those who have contributed to the successful completion of this research study titled "Structural and Magnetic Properties of $AgInX_2$ (X = S, Se, Te) Using First-Principles Calculations." I am deeply thankful to my research guide and faculty members for their invaluable guidance, continuous encouragement, and expert advice throughout the course of this study. Their knowledge, support, and constructive suggestions greatly enhanced the quality and scientific rigor of this research. I would also like to acknowledge the contributions of researchers and scientists in the fields of condensed matter physics, materials science, computational chemistry, and density functional theory (DFT), whose pioneering work and published literature provided the theoretical and methodological foundation for this study.

Financial support and sponsorship

Nil.

Conflicts of interest

The authors declare that there are no conflicts of interest regarding the publication of this paper.

References

1. S.-H. Wei, S. B. Zhang, and A. Zunger, Phys. Rev. B 59, R2478 (1999).
2. J. E. Jaffe and A. Zunger, Phys. Rev. B 28, 5822 (1983).
3. L. Mandal et al., J. Phys. Chem. Solids 65, 1769 (2004).
4. T. Torimoto et al., Adv. Mater. 22, 1163 (2010).
5. R. Miao, J. Zhu, and Y. Hou, J. Mater. Chem. C 9, 5714 (2021).
6. B. Dimmock and H. Rubin, Phys. Rev. 148, 855 (1966).
7. M. A. Islam et al., Sol. Energy Mater. Sol. Cells 195, 172 (2019).
8. S. Siebentritt and U. Rau (Eds.), Wide-Gap Chalcopyrites, Springer, Berlin (2006).
9. W. Bensouici et al., J. Alloys Compd. 789, 941 (2019).
10. A. Bahari and M. Moradi, Comput. Condens. Matter 9, 27 (2016).
11. J. L. Shay and J. H. Wernick, Ternary Chalcopyrite Semiconductors, Pergamon, Oxford (1975).
12. A. Zunger, S.-H. Wei, A. G. Petukhov, and J. E. Jaffe, J. Appl. Phys. 84, 4043 (1998).
13. P. Giannozzi et al., J. Phys.: Condens. Matter 21, 395502 (2009).
14. P. Giannozzi et al., J. Chem. Phys. 152, 154105 (2020).
15. D. R. Hamann, Phys. Rev. B 88, 085117 (2013).
16. M. van Setten et al., Comput. Phys. Commun. 226, 39 (2018).
17. X. Gonze et al., Comput. Phys. Commun. 248, 107042 (2020).
18. J. P. Perdew, K. Burke, and M. Ernzerhof, Phys. Rev. Lett. 77, 3865 (1996).
19. M. J. van Setten et al., Comput. Phys. Commun. 226, 39 (2018).
20. J. Heyd, G. E. Scuseria, and M. Ernzerhof, J. Chem. Phys. 118, 8207 (2003); 124, 219906(E) (2006).
21. A. V. Krukau, O. A. Vydrov, A. F. Izmaylov, and G. E. Scuseria, J. Chem. Phys. 125, 224106 (2006).
22. H. J. Monkhorst and J. D. Pack, Phys. Rev. B 13, 5188 (1976).
23. N. Marzari, D. Vanderbilt, A. De Vita, and M. C. Payne, Phys. Rev. Lett. 82, 3296 (1999).
24. R. Fletcher, Practical Methods of Optimization, 2nd ed., Wiley, Chichester (1987).
25. F. Birch, Phys. Rev. 71, 809 (1947).
26. A. Dal Corso, Comput. Mater. Sci. 95, 337 (2014).
27. R. Hill, Proc. Phys. Soc. A 65, 349 (1952).
28. F. Aryasetiawan and O. Gunnarsson, Rep. Prog. Phys. 61, 237 (1998).
29. C. Cococcioni and S. de Gironcoli, Phys. Rev. B 71, 035105 (2005).
30. A. Marini, G. Onida, and R. Del Sole, Phys. Rev. Lett. 88, 016403 (2002).
31. S. Lany and A. Zunger, Phys. Rev. B 78, 235104 (2008).
32. ICSD Entry 29095, FIZ Karlsruhe (2023).
33. P. Chen et al., J. Phys. D: Appl. Phys. 42, 075408 (2009).
34. Z. H. Levine and D. C. Allan, Phys. Rev. Lett. 66, 41 (1991).

35. J. C. Phillips, Rev. Mod. Phys. 42, 317 (1970).
36. I. Tsuji et al., J. Phys. Chem. B 109, 7323 (2005).
37. S. Krystеva et al., Cryst. Res. Technol. 40, 981 (2005).
38. S. N. Rashkeev and W. R. L. Lambrecht, Phys. Rev. B 63, 165212 (2001).
39. A. Villagrán-Muniz et al., Thin Solid Films 517, 2143 (2009).
40. D. Abeysinghe et al., Chem. Mater. 27, 7099 (2015).
41. M. Souilah et al., Thin Solid Films 516, 7062 (2008).
42. E. Rusu et al., Thin Solid Films 519, 7198 (2011).
43. S.-H. Wei and A. Zunger, Phys. Rev. B 37, 8958 (1988).
44. P. Dufek, P. Blaha, and K. Schwarz, Phys. Rev. Lett. 75, 3545 (1995).
45. G. F. Koster et al., Properties of the Thirty-Two Point Groups, MIT Press (1963).
46. E. L. Peltzer y Blancá et al., Phys. Rev. B 48, 15712 (1993).
47. W. A. Harrison, Electronic Structure and the Properties of Solids, W. H. Freeman, San Francisco (1980).
48. M. Lannoo and J. Bourgoin, Point Defects in Semiconductors I, Springer, Berlin (1981).
49. H. J. Hsu et al., Phys. Rev. B 85, 245201 (2012).
50. J.-H. Yang et al., Phys. Rev. B 81, 075207 (2010).
51. S. Chen et al., Adv. Mater. 25, 1522 (2013).
52. M. Born and K. Huang, Dynamical Theory of Crystal Lattices, Clarendon, Oxford (1954).
53. S. F. Pugh, Philos. Mag. 45, 823 (1954).
54. D. G. Pettifor, Mater. Sci. Technol. 8, 345 (1992).
55. A. Ganguly et al., Phys. Rev. B 78, 064302 (2008).
56. B. Elidrissi Moubtassim et al., Phys. Status Solidi B 249, 1916 (2012).
57. N. Bloembergen, Nonlinear Optics, Benjamin, New York (1965).
58. G. C. Bhar et al., Appl. Phys. Lett. 82, 2688 (2003).
59. J. H. Van Vleck, The Theory of Electric and Magnetic Susceptibilities, Oxford Univ. Press (1932).
60. L. Pauling, The Nature of the Chemical Bond, Cornell Univ. Press, Ithaca (1960).
61. T. H. Hsieh et al., Nat. Commun. 3, 982 (2012).
62. Y. Ando and L. Fu, Annu. Rev. Condens. Matter Phys. 6, 361 (2015).
63. S.-H. Wei, L. G. Ferreira, and A. Zunger, Phys. Rev. B 45, 2533 (1992).
64. Z. H. Levine, Phys. Rev. B 49, 4532 (1994).
65. V. I. Gavrilenko and R. Q. Wu, Phys. Rev. B 61, 2632 (2000).
66. S. Curtarolo et al., Nat. Mater. 12, 191 (2013).
67. C. Oses, C. Toher, and S. Curtarolo, Nat. Rev. Mater. 5, 331 (2020).
68. A. Jain et al., APL Mater. 1, 011002 (2013).
69. K. T. Butler et al., Nature 559, 547 (2018).
70. F. Bechstedt, Many-Body Approach to Electronic Excitations, Springer, Berlin (2015).